Nuclear Inst. and Methods in Physics Research, A 967 (2020) 163826

Contents lists available at ScienceDirect

Nuclear Inst. and Methods in Physics Research, A

journal homepage: www.elsevier.com/locate/nima

Calibration of large neutron detection arrays using cosmic rays

K. Zhu [a,b,*], M.B. Tsang [a,b,**], D. Dell'Aquila [a], K.W. Brown [a], Z. Chajecki [c], W.G. Lynch [a,b], S. Sweany [a,b], F.C.E. Teh [a,b], C.Y. Tsang [a,b], C. Anderson [a], A. Anthony [a,b], J. Barney [a,b], J. Crosby [a], J. Estee [a,b], I. Gasparic [d], G. Jhang [a], O.B. Khanal [c], S. Kodali [a], J. Manfredi [a,b], C.Y. Niu [a], R.S. Wang [a]

[a] National Superconducting Cyclotron Laboratory, Michigan State University, East Lansing, MI 48824, USA
[b] Department of Physics and Astronomy, Michigan State University, East Lansing, MI 48824, USA
[c] Department of Physics, Western Michigan University, Kalamazoo, MI 49008, USA
[d] Division of Experimental Physics, Rudjer Boskovic Institute, Zagreb, Croatia

ARTICLE INFO

Keywords:
Neutron detector
Calibration
Cosmic rays
NE-213

ABSTRACT

Cosmic muons are used to calibrate the position, light output and the relative timing offset of the Large Area Neutron Array (LANA). Each 2 × 2 m^2 LANA wall consists of twenty-five horizontal neutron detection bars. Each bar is 2 m long with a cross-section of 6.35×7.62 cm^2 Pyrex container filled with NE-213 organic scintillation liquid. The average position and time resolution of a bar is found to be about 8 cm and 500 ps FWHM, respectively. Our method provides an accurate, fast and convenient calibration of LANA that can be applied to general scintillation arrays without the use of radioactive sources or beams.

1. Introduction

Neutrons are produced in nearly all nucleus–nucleus collisions. They yield important information about nuclear structure as well as dynamics of nuclear reactions. Thus, in recent years more and more dedicated neutron arrays have been incorporated into new generation of nuclear physics experiments [1–13].

Due to the relatively low interaction probability, detection of fast neutrons represents a considerable technical challenge. Typically, calibration of a neutron detector requires the use of radioactive sources that produce gamma rays with well-known energies [1,14]. Nearly all of these sources have low energy gamma <5 MeV. Furthermore, for large detector array, calibration has to be done at various positions of individual detector to determine the position dependence of the light collection of the photo-multipliers incorporated in the neutron detectors. Such procedures are tedious and time-consuming especially when the area of the arrays is large. Alternatively one can use nuclear reactions that produce neutrons at fixed energies for calibrations. The latter method requires accelerated ion beams which may not be readily available [15,16].

The purpose of this paper is to describe a method that uses high-energy muons produced in cosmic-ray showers to calibrate the light response of a large neutron array [17–20]. The mean muon energy is ≈ 2GeV [21]. Our work also shows how the time and position resolutions of the array can be obtained and how to match the time difference of each neutron detector without an external timing detector. We illustrate our method with the Large Area Neutron Array (LANA) constructed at the National Superconducting Cyclotron Laboratory [1] but the method is general and can be applied to other neutron detectors. LANA has been used in many nuclear experiments [22–24]. Its properties including the position and time resolution have been characterized in Ref. [1] with radioactive source and beam. When appropriate, we will compare our results to that from Ref. [1].

This paper is organized as follows: After a brief introduction, Section 2 describes the setup of LANA and associated electronics. Section 3 discusses the position and time resolution of the bars by using cosmic muons. It also describes a procedure to obtain the relative time offsets between different scintillation bars in LANA. Section 4 shows how signals produced by cosmic rays can be used to characterize the attenuation length of each bar and the procedure to match the gain of photomultipliers on opposite end of a scintillation bar. Section 5 is dedicated to the light-output calibration procedure, including the position dependent corrections. Finally, our work is summarized in Section 6.

2. Experimental setup: The large area neutron array

The Large Area Neutron Array (LANA) is composed of two large neutron walls, each of which consists of 25 independent detection cells

* Corresponding author at: National Superconducting Cyclotron Laboratory, Michigan State University, East Lansing, MI 48824, USA.
** Corresponding author.
E-mail addresses: zhuk@nscl.msu.edu (K. Zhu), tsang@nscl.msu.edu (M.B. Tsang).

https://doi.org/10.1016/j.nima.2020.163826
Received 26 October 2019; Received in revised form 1 March 2020; Accepted 18 March 2020
Available online 21 March 2020
0168-9002/

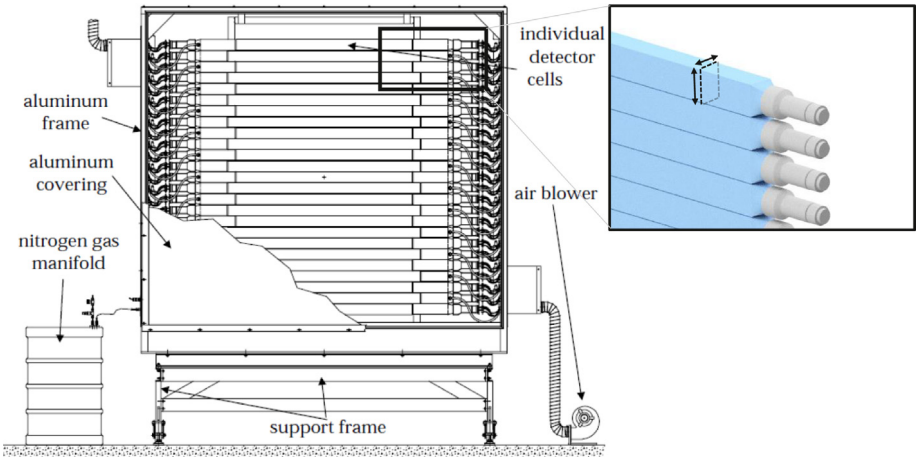

Fig. 1. Schematic drawing of one wall of the Large Area Neutron Array.
Source: This drawing is adapted from Ref. [1].

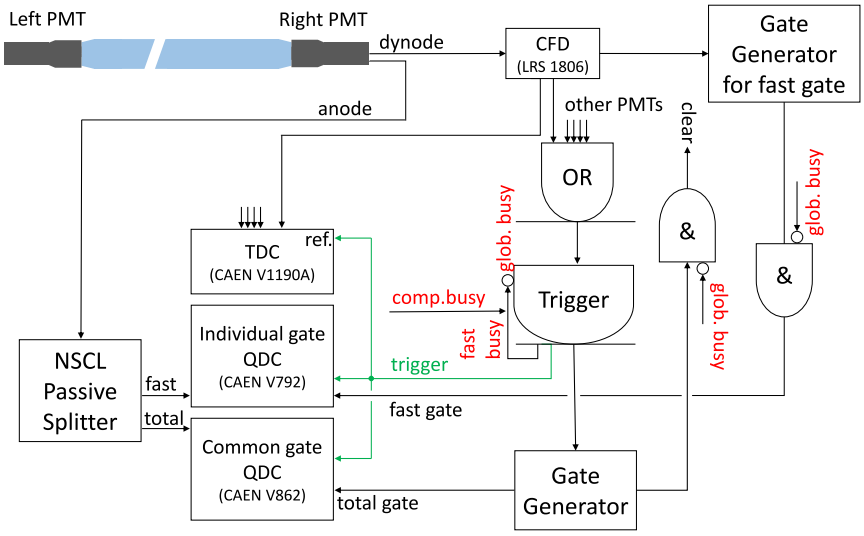

Fig. 2. Schematic of the electronics setup (for one PMT) used to process signals from the Neutron Walls when the wall is used in standalone mode. An exact reproduction of these circuits are used to process signals obtained with each of the 100 individual PMTs. "Fast" and "total" are two copies of the original anode signal but integrated respectively by using a fast gate (containing only the fast component of the signal) and total gate (containing the whole signal) for PSD analysis. PMT dynode signals are used for timing.

that cover a total area of 2×2 m^2. Each detector cell is a 2 m-long Pyrex glass container, with a rectangular cross section of height $h = 7.62$ cm on the vertical direction and depth $w = 6.35$ cm as indicated in the upper corner of Fig. 1, filled with liquid organic scintillator NE-213. To maximize detection efficiency, the LANA features large active detection area, small dead space between scintillators and minimum amount of inactive mass through which the neutrons must pass [1]. For heavy ion collision experiments, it is designed to detect neutron from about 10 MeV to about 300 MeV when it is placed at 4.5 m from the target. Despite recent advance in new scintillation materials, liquid scintillator is still the most cost effective way to build large area neutron detectors. NE-213 was chosen for its excellent efficiency for detecting fast neutrons and its pulse shape discrimination (PSD) properties that enable the discrimination between neutrons and gamma-rays [25,26]. Its PSD characteristic is especially desirable for heavy-ion collision experiments where copious photons and neutrons are produced and must be identified in data analysis. Both ends of each Pyrex bar are coupled with 7.5 cm diameter Philips Photonics XP4312B/04 photomultipliers (PMTs), to detect the scintillating light produced in the bar by an incident radiation. Typical high voltage employed on PMTs is 2200 V. The scintillator bars are horizontally stacked as schematically shown in Fig. 1. Taking into account the thickness of the Pyrex glass (3 mm) and a gap of 3 mm between bars, the total active geometrical area of the 2×2 m^2 wall is reduced by about 12% [1].

The physical location of each bar is determined by laser measurements made on the surface of the wall with respect to a global reference frame in the Facility for Rare Isotope Beams (FRIB) Laboratory [27]. Such measurements allow one to determine not only the absolute position of each bar with respect to the target during an experiment, but also the relative positions between bars of each wall, which is relevant for the time calibrations described below.

In order to implement the detector capabilities described above, we used the electronics setup schematically shown in Fig. 2 for one PMT. An analogous electronics chain is replicated for each of the 100 PMTs in the two neutron walls. Each PMT has an embedded passive voltage divider circuit as described in Ref. [1]. Such a circuit, omitted in the drawing of Fig. 2 for the sake of clarity, allows one to use both the anode and the last dynode signals, labeled respectively as "anode" and "dynode" in the figure. The anode signal is a negative-voltage pulse that contains the charge from the multiplier chain and is used to produce the integrated charge signals. To enable the PSD analysis, the anode signal is initially split into two equal signals by means of an NSCL passive splitter module. One split signal, named "total" in

Fig. 2, is sent to a channel of a common gate CAEN V792 charge-to-digital converter (QDC) [28] for the integration of the total charge. The other split signal is integrated for its fast component (≈30 ns). To successfully implement the detection of more than a single particle in an event, which is required for high-multiplicity heavy-ion collision experiments, the gate for the fast component integration is generated independently for each hit within an event. The gate is generated from the dynode signals by using a Lecroy 1806 16-channel constant-fraction discriminator (CFD) [29] and a CAEN C469 16-channel gate and delay generator [28]. These gates are used to digitize the fast component of the anode signals using a CAEN V862 individual gated QDC [28]. This allows the PSD technique to be applied exclusively to single-particle events. The logic chain, which includes trigger, gates, and timing, is implemented by using the dynode signal from the PMT voltage divider fed into the CFDs. The trigger to the acquisition system is produced by a logical "OR" of all the CFD signals for each PMT in the walls in anti-coincidence with a global busy signal, generated as the "OR" of the computer busy and a fast busy signal, obtained by stretching a copy of the trigger itself. The latter prevents multiple triggers at a time interval shorter than the time required by the circuit to generate the gates and to process the event. The trigger signal is used to produce the total gate for the commonly gated QDCs, which is a logic signal of about 3 μs in length, as well as the time reference and trigger signals for the CAEN V1190A time-to-digital converter (TDC) [28]. This TDC records the time difference between the individual dynode CFD signal and this reference signal, which are used for the position and time calibrations of the wall. Finally the trigger is sent to the data acquisition to enable the readout of each module. In the latest experiment using LANA, digital electronics was set up in parallel to the analog electronics for 8 bars. Analysis using digitized waveforms to devise software algorithm to improve neutron/gamma pulse shape discrimination (PSD) is discussed in Ref. [26].

3. Position and time offset calibration

3.1. Impact position calibration

When an ionizing radiation strikes one of the bars of the neutron wall, scintillation light is isotropically produced in the NE-213 liquid scintillator along the ionization path. The horizontal X-position of the hit is extracted by comparing the time signals recorded by the PMTs at the two ends of the bar, while the vertical Y-position is constrained by the physical dimension of the scintillation fluid inside the bar.

Given t_{left} and t_{right} as the absolute times which correspond ideally to the arrival times of the scintillation light at the left and right PMT photocathodes, the horizontal position of the particle hit along the bar, with respect to the bar center, is given by:

$$X = \frac{t_{\text{left}} - t_{\text{right}} - \tau}{2}\bar{v} \tag{1}$$

where $\bar{v}$ is the average horizontal speed of the light propagating through the bar and τ is the residual delay since the timing for the left and right PMT and electronics channels are not exactly the same due to different cable length, different delays in electronic channels or modules etc. Because the cosmic rays hit the neutron wall bars with no preference, the hit distribution along one bar should be uniform. The time difference, $\Delta t = t_{\text{left}} - t_{\text{right}}$ distribution is shown in the top panel of Fig. 3 for bar #8 of the LANA walls. As expected, the distribution is almost flat with two sharp edges, corresponding to the geometrical left and right ends of the bar. In order to determine the left and right edge consistently for all the bars, we perform a numerical differentiation of the time difference spectrum. The result exhibits two sharp peaks, where the time difference differential diverges negatively at Δt_{max} or positively at Δt_{min} as shown in the bottom panel of Fig. 3. A numerical peak finding method can then be used to infer the positions of the two edges. An analogous procedure is applied to all the bars. The following

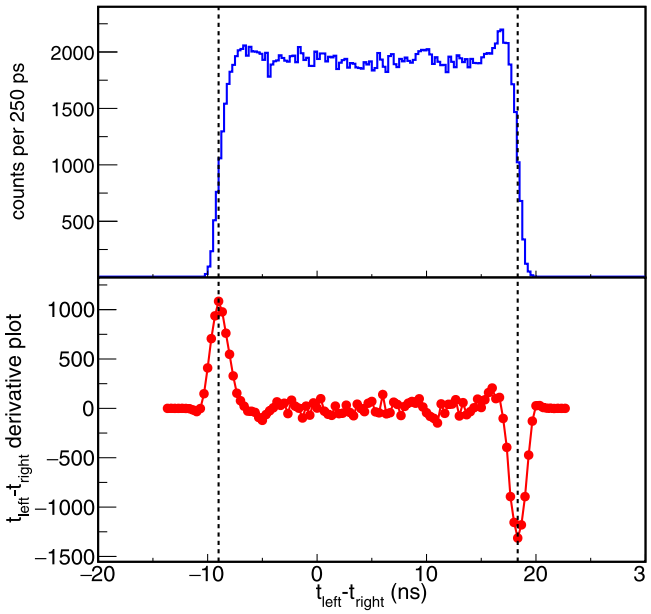

Fig. 3. (top panel) Time difference, $t_{\text{left}} - t_{\text{right}}$ distribution for cosmic muons obtained with bar #8 of the LANA. A numerical differentiation of this spectrum (bottom panel) is used to determine the position of right and left edges of the $t_{\text{left}} - t_{\text{right}}$ distribution consistently as indicated by the dashed lines, which correspond to $-\frac{L}{2}$ and $\frac{L}{2}$ respectively.

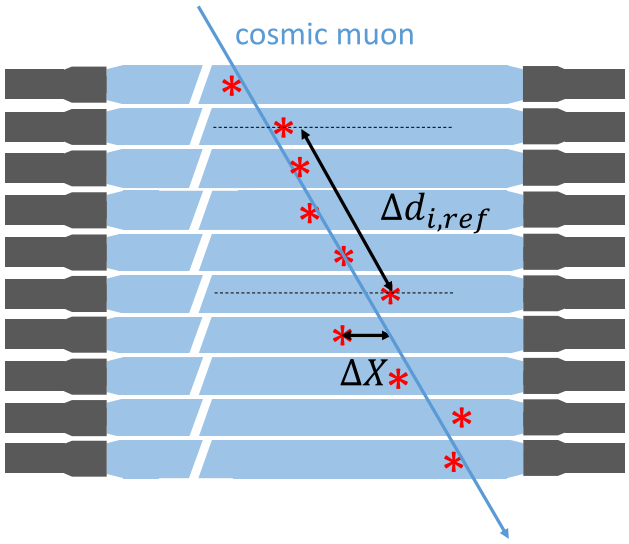

Fig. 4. A schematic drawing of a cosmic muon track penetrating 10 consecutive bars in the wall. Red stars represent the hit positions. The reconstructed muon track (blue slanted line) is obtained by fitting the measured hit positions on the bars with a straight line. ΔX indicates the position deviation between the expected and the actual hit position. $\Delta d_{i,\text{ref}}$ is the theoretical distance between two hits on a certain bar and reference bar respectively. (For interpretation of the references to color in this figure legend, the reader is referred to the web version of this article.)

equations can be used to obtain the position calibration parameter of a bar:

$$\begin{aligned} \tau &= \frac{\Delta t_{\text{max}} + \Delta t_{\text{min}}}{2} \\ \bar{v} &= \frac{2L}{\Delta t_{\text{max}} - \Delta t_{\text{min}}} \end{aligned} \tag{2}$$

where L is the bar length.

After the position is calibrated, we define a cosmic track by fitting the impact positions measured in at least ten consecutive bars as

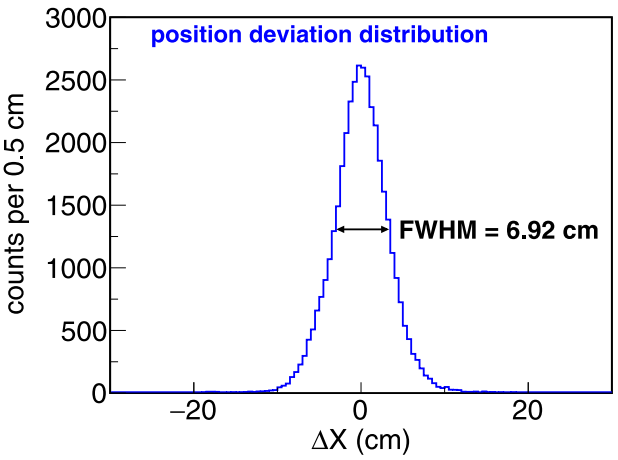

Fig. 5. Position deviation distribution for bar #8.

schematically shown in Fig. 4. (Except in Section 5, no other conditions are imposed on the cosmic tracks.) From the fitted track (blue diagonal line passing through the bars in Fig. 4) we can calculate the deviation (ΔX) between the impact position and that extracted from track reconstruction. Fig. 5 shows the ΔX distributions for Bar #8 with a FWHM of 6.92 cm. The obtained position resolution is averaged over a LANA bar. It is worse towards the end of the bar due to attenuation of the light signal from the PMT located at the opposite end. It is worth noting that the above resolutions include the uncertainty in the track reconstruction. The mean position resolution for all 25 bars is 8 ± 1.5 cm which is consistent with the position resolution obtained in Ref. [1] suggesting that the PMTs in LANA wall have not deteriorated significantly even after 25 years. The X position resolution is similar to the height of the NE-213 liquid inside the Pyrex cell (7.02 cm) which determines the Y position resolution.

3.2. Time resolution and time offset calibration

Cosmic muons travel at nearly the speed of light. As illustrated in Fig. 4, theoretically, one can calculate the expected arrival time difference of a cosmic muon track between two bars since we know the position of the bars accurately. The expected time difference of the signal recorded in a bar used as the reference and the ith bar of a wall is given by:

$$\Delta T^{\text{th}}_{i,\text{ref}} = \frac{\Delta d_{i,\text{ref}}}{v} \tag{3}$$

where $\Delta d_{i,\text{ref}}$ is the theoretical length of the cosmic muon path from the ith bar to the reference bar determined by the track fit, and $v \approx c$ is the speed of the cosmic muon. The time difference measured experimentally with TDC is given by:

$$\Delta T^{\text{exp}}_{i,\text{ref}} = \frac{(t_{\text{left}} + t_{\text{right}})_{\text{ref}}}{2} - \frac{(t_{\text{left}} + t_{\text{right}})_i}{2} + \delta_{i,\text{ref}} \tag{4}$$

where $\delta_{i,\text{ref}}$ is the time difference between bars arising from differing cable and electronic delays. Fig. 6 shows the distribution of $\Delta T_{i,\text{ref}} = \Delta T^{\text{exp}}_{i,\text{ref}} - \Delta T^{\text{th}}_{i,\text{ref}}$ for each of the bars in a LANA wall. The Y-axis is the bar number, i. Bar #12 is chosen as the reference bar with the obvious result $\Delta T_{12,12} = 0$. Deviation of $\delta_{i,\text{ref}}$ from zero suggests that time delays arising from the differences in cable and electronic delays, etc. are different for pair of bars. While we cannot determine the absolute time offset or delays for each bar, we can align the peaks of $\Delta T_{i,\text{ref}}$ to zero as shown in the lower panel of Fig. 6. Fig. 7 shows a Gaussian shape distribution of $\Delta T_{i,\text{ref}}$ for bar #8 with FWHM of 751 ps. The time resolution, FWHM, for bar #8 involving two PMTs can be deduced as: $\frac{751 \text{ ps}}{\sqrt{2}} = 531$ ps assuming the time resolutions of all the PMTs and therefore the bars are similar. The average time resolution for all 24

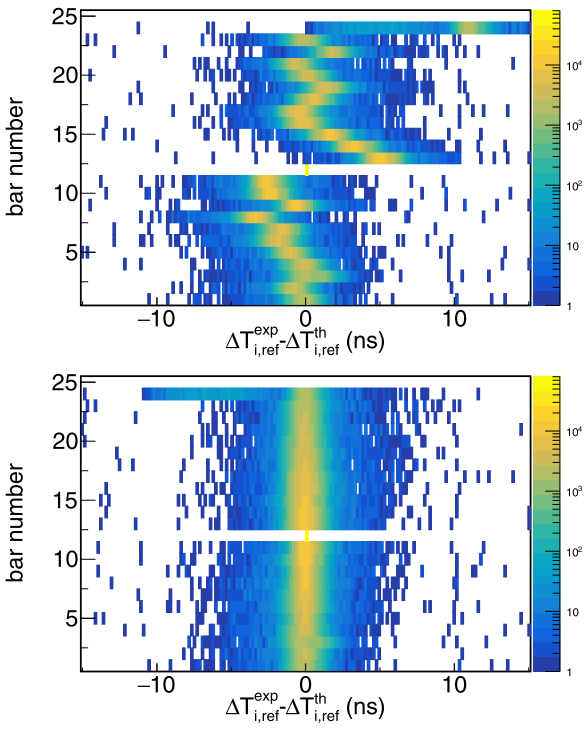

Fig. 6. $\Delta T_{i,\text{ref}}$ distributions for each of the bar in the array before (top panel) and after (bottom panel) the peaks are aligned. Y-axis is the bar number while X-axis shows the corresponding $\Delta T^{\text{exp}}_{i,\text{ref}} - \Delta T^{\text{th}}_{i,\text{ref}}$ distributions. Bar #12 is used as the reference bar; therefore $\Delta T_{12,\text{ref}} = 0$.

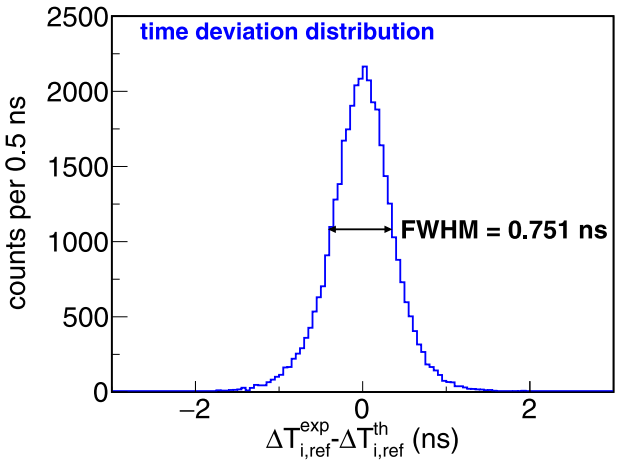

Fig. 7. Time deviation distribution for bar #8.

bars is 504 ± 106 ps. The small standard deviation of the mean justifies the asumption that the time response of the PMTs are quite similar. However, this time resolution cannot be compared directly to the time resolution of 1 ns obtained in Ref. [1] which involves the use of an external time zero Si detector.

4. Light attenuation length and gain-matching of photomultipliers

When an incident particle interacts with the NE-213 liquid, only a small fraction of the produced optical photons directly reach the PMTs. Some photons are lost completely and the rest of the photons experience multiple reflections on the surface of the Pyrex glass cell before being collected by the PMTs. The photons that reach the photocathodes are detected by the left and right PMTs attached at the end of the Pyrex

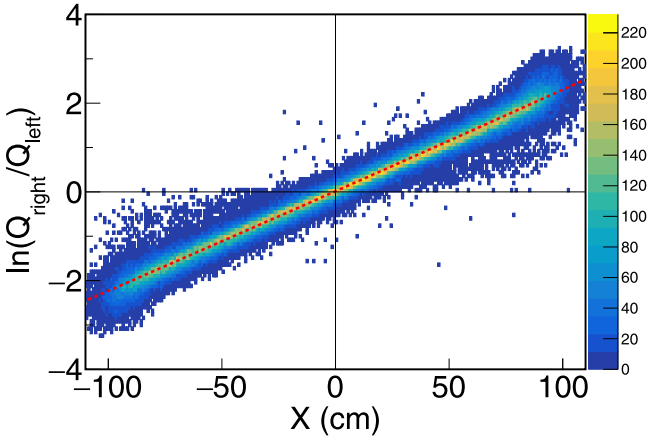

Fig. 8. Eq. (6) as a function of the position X along the bar #8 for cosmic ray data. The red dashed line is a linear fit of the distribution. The intercept of the best fit line is compatible with (0,0), indicating a good left–right matching of the PMT gains. The slope allows to extract the attenuation length of the bar.

tubes and converted to charge by the QDC in Fig. 2. The measured charge is a function not only of the number of photons produced by the incident particle (and therefore of the energy deposited by the particle in the material) but also of the hit position X as described below:

$$\begin{aligned} Q_{\text{right}}(N,X) &= g_{\text{right}}\frac{N}{2}e^{-\frac{L/2-X}{\lambda}} \\ Q_{\text{left}}(N,X) &= g_{\text{left}}\frac{N}{2}e^{-\frac{L/2+X}{\lambda}} \end{aligned} \tag{5}$$

where g_{right} and g_{left} are the gain of the corresponding PMT, L is the bar length, N is the total number of photons emitted and λ is the technical attenuation length (TDL) of the scintillator material in our detector to optical photons. TDL not only describes the self-absorption in the material but also includes the effect of geometry. λ is therefore, normally smaller than the material bulk light attenuation length, which is ~270 cm [30]. The logarithm of the ratio of Eq. (5) gives a linear expression:

$$\ln(\frac{Q_{\text{right}}}{Q_{\text{left}}})(X) = \frac{2}{\lambda}X + \ln(\frac{g_{\text{right}}}{g_{\text{left}}}) \tag{6}$$

with a slope equal to $\frac{2}{\lambda}$ and an intercept $\ln(\frac{g_{\text{right}}}{g_{\text{left}}})$. Fig. 8 plots the gain ratio of the two PMTs $\ln(\frac{Q_{\text{right}}}{Q_{\text{left}}})(X)$ as a function of X for bar #8. The distribution is mostly linear with some curvature at large absolute X values due to the light collection efficiency near the end of the bar. The red dashed line is the result of a linear fit of data from −90 cm to 90 cm to avoid any possible effect near the end of the bar. We have varied the range of fit from (−80 cm, 80 cm) to (−90 cm, 90 cm) and find that the fitting results are stable to within 1%. The mean λ value for all the bars in the array is 94 ± 8 cm. Thus the light attenuation effects are significant in the LANA, due to its size and geometry.

The intercept of Eq. (6) is the left–right gain ratio and can be used to facilitate matching the gain of left and right PMTs of each bar using the following procedure. A cosmic ray run is performed to produce a plot similar to Fig. 8. Using the power-law of the high voltage (HV), gain ~ $(HV)^N$, (e.g. $N \sim 8$ for LANA) a new gain setting is chosen to minimize the intercept. It takes about 3 iterations to adjust and match all HV for 100 PMTs in LANA in order to consistently equalize the PMT gains for all the bars with $(\frac{g_{\text{right}}}{g_{\text{left}}})$, close to one. One can also use the vanishing intercept in Eq. (6) to judge the quality of the gain matching in offline analysis. In our case, the statistics from an overnight run is sufficient for one iteration. The same method can also be used between experimental runs to monitor the gain of the neutron detection array.

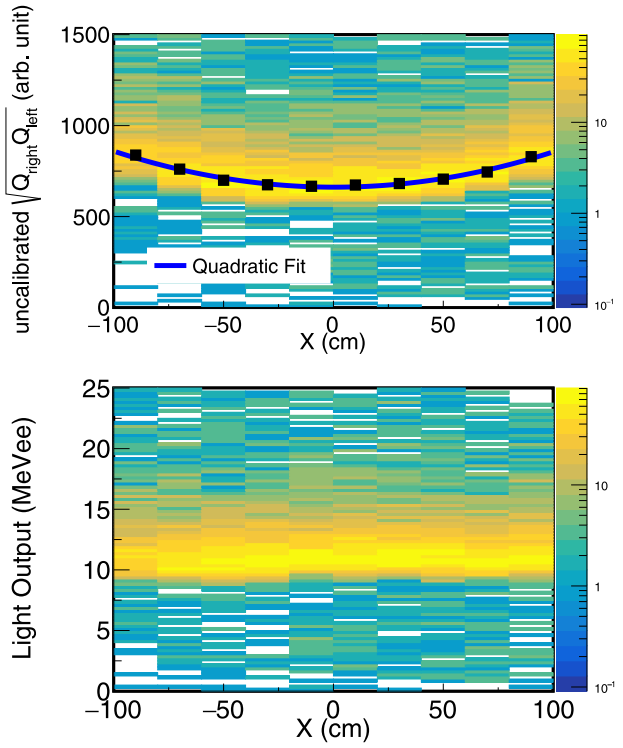

Fig. 9. (Top panel) Uncalibrated left–right GM as a function of the position along bar #8. Vertical cosmic rays are selected by restricting data to those with impinging angles $-10° \leq \theta \leq 10°$ with respect to the axis perpendicular to the horizontal central axis of the bar. Black points are the position of the cosmic ray MPV deduced with a Landau fit of data for each position bin. The blue line is the result of a quadratic fit of the cosmic MPV position dependence. (Bottom panel) Same as top panel after light calibration and position dependency correction.

5. Light output calibration and position corrections

In order to calculate the neutron detection efficiency from simulation, we need to know the neutron light output threshold accurately. We use cosmic muons to calibrate neutron signal light output to MeV electron equivalent (MeVee). Cosmic muons reaching the sea level have a mean energy of 2 GeV [18,20,21]. The most probable energy deposited in the scintillator material by such muons depends on the length of their path in the material. We simulate the interaction of 2 GeV muons with the NE-213 material by using the GEANT4 toolkit and the standard electromagnetic physics list. Our simulation indicates that, if muons punch through the bar vertically, the expected deposited energy has a Landau distribution whose most possible value (MPV) is 11.02 MeV. To calibrate the neutron detectors, we require the incident angles of the cosmic muon track to the axis to be within 10 degree perpendicular to the horizontal central axis of the bar. This is to ensure the shortest track path in the scintillating liquid in the neutron bar to be consistent with the simulations, in order to achieve accurate determination of the energy loss by the cosmic muons. The 10 degree condition is chosen so that the uncertainties of transverse length of the track in a bar is consistent with the position resolution of the bars.

To minimize the position dependence, the geometric means (GM) of the charges in the left and right PMTs defined below is typically used for the energy-light calibrations of neutron detectors:

$$\sqrt{Q_{\text{left}}(N,X)Q_{\text{right}}(N,X)} = f(N) = \frac{N}{2}\sqrt{g_{\text{left}}g_{\text{right}}e^{-L/\lambda}} \tag{7}$$

Fig. 9 shows the GM distributions of bar #8 with a bin width of 20 cm. Consistent with the GEANT4 simulations, the GM distribution shown in Fig. 10 has a Landau shape. The black squares in Fig. 9 (top panel) show the MPV of the Landau GM distributions of vertically-penetrating

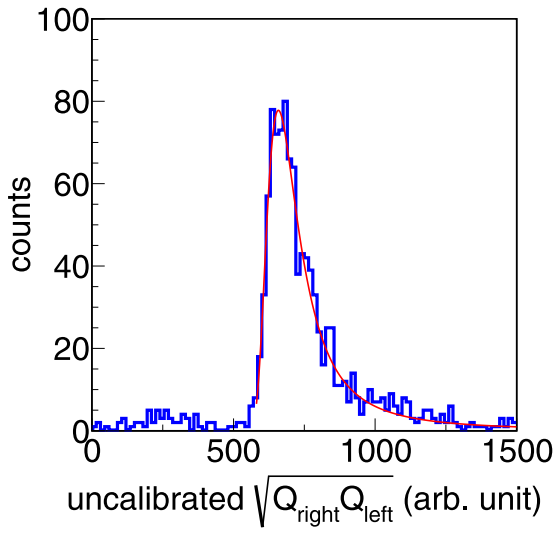

Fig. 10. An example of a Landau fit of the GM distribution for the position bin −20 cm ≤ X ≤ 0 cm.

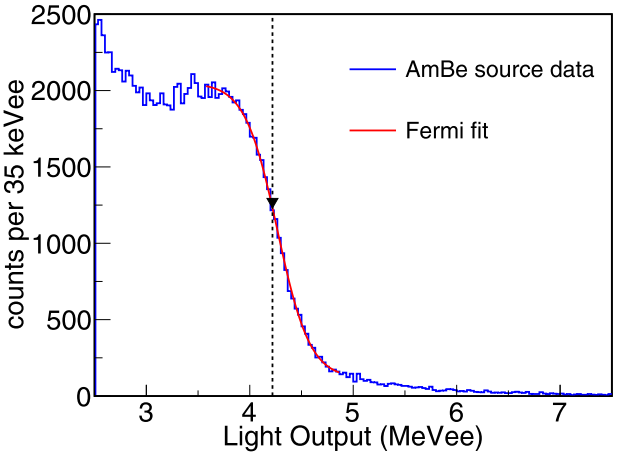

Fig. 11. Position corrected light output spectrum obtained with an AmBe source for bar #8. The Compton edge is fitted with a Fermi function and the deduced position associated to the 4.44 MeV transition in ^{12}C is indicated by an arrow and a dashed line. The theoretical value of the Compton edge is 4.2 MeV.

cosmic rays as a function of X position. The statistical uncertainties of the black squares are smaller than the size of the marker. Despite using the GM of Eq. (7), there is still some position dependence, most likely coming from the position dependence of the light collection due to scattering and reflections along the bar. This residual position dependence can be corrected empirically by flattening the experimental GM distribution for each X position using a parabolic fit of MPV (blue line in Fig. 9 (top panel)). The flattened or corrected GM vs X-position spectrum is shown in Fig. 9 (bottom panel), where the MPV of the GM has been calibrated to 11.02 MeVee.

To validate the cosmic ray energy-light calibration procedure, we placed an intense Americium-Beryllium (AmBe) neutron source at a distance of about 60 cm from the front of the LANA walls. Such source emits a mono-energetic 4.44 MeV gamma-ray from the reaction of $\alpha + {}^{9}\mathrm{Be} \rightarrow n + {}^{12}\mathrm{C}^{*}$. A typical AmBe gamma spectrum obtained with bar #8 is shown in Fig. 11. The sharp Compton edge expected to lie at 4.2 MeV, can be easily defined by fitting it with the sum of a Fermi function and a linear background. The Fermi function is of the form $f(x) = \frac{a_0}{\exp\frac{x-a_1}{a_2}+1}$, where a_0, a_1, a_2 are free parameters. The position of the Compton edge is determined from the a_1 parameter by using

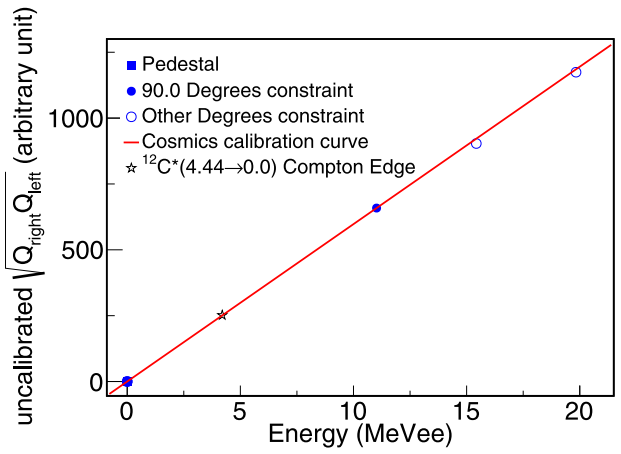

Fig. 12. The cosmic-ray energy-light calibration curve (red line) obtained by using the 11.02 MeVee constraint of the cosmic muons and the zero-offset (blue solid circle and blue square, respectively). The open star corresponds to the Compton edge discussed in Fig. 11. The open blue circles are two additional light-energy calibration points obtained by select cosmic muons that punch through the detector at 44.4 ± 5 and 56.3 ± 5 degrees with respect to the axis perpendicular to the bar length.

the method proposed in Ref. [31]. The open star in Fig. 12 shows that the 4.2 MeV from the Compton edge calibration lies along the red line obtained from the cosmic calibration at 11.02 MeVee and the zero offset of the electronics confirming the validity of our calibration procedure. The statistical uncertainties of the blue square, open star and blue circle points are smaller than the size of the marker in Fig. 12.

By selecting cosmic tracks at large incidence angle, the calibration can be extended to higher energy depositions. We select cosmic muons that punch through the detector at 44.4 ± 5 and 56.3 ± 5 degrees with respect to the axis perpendicular (0 deg) to the bar length. According to the GEANT4 simulations, such muons should deposit 15.4 and 19.8 MeV. These points are added to Fig. 12 as the blue open circles. It appears that the light response remains linear out to 20 MeV.

6. Conclusion

In summary, we describe the calibration of a large area neutron array using high-energy muons produced in cosmic ray showers. The methods have been successfully applied to LANA, the NE-213 scintillator-based neutron walls constructed at the National Superconducting Cyclotron Laboratory. The cosmic muon allows us to obtain position and time offset calibration of individual bars in the array. Typical position and time resolutions of a LANA bar are found, respectively, to be 8 cm and 500 ps FWHM. These measurements serve as benchmarks for future upgrade of the LANA. Calibration with the cosmic-ray muons also allows us to correct for the position dependence of the light response along the bar. The energy-light calibration obtained with the cosmic muon and an AmBe radioactive source is linear. We also present a procedure to perform gain matching of the PMTs with cosmic data.

Declaration of competing interest

The authors declare that they have no known competing financial interests or personal relationships that could have appeared to influence the work reported in this paper.

CRediT authorship contribution statement

K. Zhu: Software, Validation, Formal analysis, Investigation, Resources, Data curation, Writing - original draft, Writing - review & editing, Visualization. **M.B. Tsang:** Conceptualization, Validation, Investigation, Writing - review & editing, Supervision, Visualization, Project

administration, Funding acquisition. **D. Dell'Aquila:** Software, Formal analysis, Investigation, Data curation, Writing - original draft. **K.W. Brown:** Software, Investigation, Resources, Writing - review & editing. **Z. Chajecki:** Software, Investigation, Resources, Funding acquisition. **W.G. Lynch:** Conceptualization, Investigation, Validation, Supervision, Project administration, Funding acquisition. **S. Sweany:** Investigation. **F.C.E. Teh:** Investigation, Validation. **C.Y. Tsang:** Software, Investigation. **C. Anderson:** Resources. **A. Anthony:** Investigation. **J. Barney:** Investigation. **J. Crosby:** Resources. **J. Estee:** Investigation. **I. Gasparic:** Resources. **G. Jhang:** Investigation. **O.B. Khanal:** Investigation, Resources. **S. Kodali:** Resources. **J. Manfredi:** Investigation. **C.Y. Niu:** Resources. **R.S. Wang:** Validation, Resources.

Acknowledgments

This work is supported by the US National Science Foundation under Grant No. PHY-1565546 and the U.S. Department of Energy (Office of Science) under Grant Nos. DE-SC0014530, DE-NA0002923.

References

[1] P. Zecher, A. Galonsky, J. Kruse, S. Gaff, J. Ottarson, J. Wang, F. Deák, A. Horváth, A. Kiss, Z. Seres, K. Ieki, Y. Iwata, H. Schelin, A large-area, position-sensitive neutron detector with neutron/γ-ray discrimination capabilities, Nucl. Instrum. Methods Phys. Res. A 401 (2) (1997) 329–344, http://dx.doi.org/10.1016/S0168-9002(97)00942-X, URL http://www.sciencedirect.com/science/article/pii/S016890029700942X.

[2] T. Blaich, T. Elze, H. Emling, H. Freiesleben, K. Grimm, W. Henning, R. Holzmann, G. Ickert, J. Keller, H. Klingler, W. Kneissl, R. Konig, R. Kulessa, J. Kratz, D. Lambrecht, J. Lange, Y. Leifels, E. Lubkiewicz, M. Proft, W. Prokopowicz, C. Schuter, R. Schmidt, H. Spies, K. Stelzer, J. Stroth, W. Walus, E. Wajda, H. Wollersheim, M. Zinser, E. Zude, A large area detector for high-energy neutrons, Nucl. Instrum. Methods Phys. Res. A 314 (1) (1992) 136–154, http://dx.doi.org/10.1016/0168-9002(92)90507-Z, URL http://www.sciencedirect.com/science/article/pii/016890029290507Z.

[3] The R^3B Collaboration, NeuLAND technical report, 2011, URL https://edms.cern.ch/ui/file/1865739/1/TDR_R3B_NeuLAND_public.pdf.

[4] B. Luther, T. Baumann, M. Thoennessen, J. Brown, P. DeYoung, J. Finck, J. Hinnefeld, R. Howes, K. Kemper, P. Pancella, G. Peaslee, W. Rogers, S. Tabor, MoNA—The modular neutron array, Nucl. Instrum. Methods Phys. Res. A 505 (1) (2003) 33–35, http://dx.doi.org/10.1016/S0168-9002(03)01014-3, Proceedings of the tenth Symposium on Radiation Measurements and Applications. URL http://www.sciencedirect.com/science/article/pii/S0168900203010143.

[5] T. Baumann, J. Boike, J. Brown, M. Bullinger, J. Bychoswki, S. Clark, K. Daum, P. DeYoung, J. Evans, J. Finck, N. Frank, A. Grant, J. Hinnefeld, G. Hitt, R. Howes, B. Isselhardt, K. Kemper, J. Longacre, Y. Lu, B. Luther, S. Marley, D. McCollum, E. McDonald, U. Onwuemene, P. Pancella, G. Peaslee, W. Peters, M. Rajabali, J. Robertson, W. Rogers, S. Tabor, M. Thoennessen, E. Tryggestad, R. Turner, P. VanWylen, N. Walker, Construction of a modular large-area neutron detector for the NSCL, Nucl. Instrum. Methods Phys. Res. A 543 (2) (2005) 517–527, http://dx.doi.org/10.1016/j.nima.2004.12.020, URL http://www.sciencedirect.com/science/article/pii/S0168900205000379.

[6] Z.-H. Yang, Y.-L. Ye, J. Xiao, H.-B. You, H.-N. Liu, Y.-L. Sun, Z.-H. Wang, J. Chen, Fast calibration methods using cosmic rays for a neutron detection array, Chin. Phys. C 36 (3) (2012) 222–227, http://dx.doi.org/10.1088/1674-1137/36/3/006.

[7] Z. Yang, H. You, J. Xiao, Y. Ye, Performance calibration using cosmic rays for the multi-neutron correlation spectrometer, Plasma Sci. Technol. 14 (6) (2012) 464–468, http://dx.doi.org/10.1088/1009-0630/14/6/06.

[8] W. Peters, S. Ilyushkin, M. Madurga, C. Matei, S. Paulauskas, R. Grzywacz, D. Bardayan, C. Brune, J. Allen, J. Allen, Z. Bergstrom, J. Blackmon, N. Brewer, J. Cizewski, P. Copp, M. Howard, R. Ikeyama, R. Kozub, B. Manning, T. Massey, M. Matos, E. Merino, P. O'Malley, F. Raiola, C. Reingold, F. Sarazin, I. Spassova, S. Taylor, D. Walter, Performance of the versatile array of neutron detectors at low energy (VANDLE), Nucl. Instrum. Methods Phys. Res. A 836 (2016) 122–133, http://dx.doi.org/10.1016/j.nima.2016.08.054, URL http://www.sciencedirect.com/science/article/pii/S0168900216308816.

[9] C. Langer, A. Algora, A. Couture, M. Csatlós, J. Gulyás, M. Heil, A. Krasznahorkay, J. O'Donnell, R. Plag, R. Reifarth, L. Stuhl, K. Sonnabend, T. Tornyi, F. Tovesson, Simulations and developments of the low energy neutron detector array LENA, Nucl. Instrum. Methods Phys. Res. A 659 (1) (2011) 411–418, http://dx.doi.org/10.1016/j.nima.2011.06.079, URL http://www.sciencedirect.com/science/article/pii/S0168900211012484.

[10] P. Rout, D. Chakrabarty, V. Datar, S. Kumar, E. Mirgule, A. Mitra, V. Nanal, R. Kujur, A large area plastic scintillator detector array for fast neutron measurements, Nucl. Instrum. Methods Phys. Res. A 598 (2) (2009) 526–533, http://dx.doi.org/10.1016/j.nima.2008.09.034, URL http://www.sciencedirect.com/science/article/pii/S016890020801406X.

[11] P. Sugathan, A. Jhingan, K. Golda, T. Varughese, S. Venkataramanan, N. Saneesh, V. Satyanarayana, S. Suman, J. Antony, R. Shanti, K. Singh, S. Saini, A. Gupta, A. Kothari, P. barua, R. Kumar, J. Zacharias, R. Singh, B. Behera, S. Mandal, I. Govil, R. Bhowmik, Neutron detector array at IUAC: Design features and instrumentation developments, J. Phys. 83 (5) (2014) 807–815, http://dx.doi.org/10.1007/s12043-014-0872-9, URL http://www.sciencedirect.com/science/article/pii/S016890020801406X.

[12] Jyvaskylan yliopisto, Successful test of the MONSTER spectrometer provided new nuclear structure information, 2019, URL https://phys.org/news/2019-04-successful-monster-spectrometer-nuclear.html.

[13] I. Tilquin, Y.E. Masri, M. Parlog, P. Collon, M. Hadri, T. Keutgen, J. Lehmann, P. Leleux, P. Lipnik, A. Ninane, F. Hanappe, G. Bizard, D. Durand, P. Mosrin, J. Péter, R. Régimbart, B. Tamain, Detection efficiency of the neutron modular detector DEMON and related characteristics, Nucl. Instrum. Methods Phys. Res. A 365 (2) (1995) 446–461, http://dx.doi.org/10.1016/0168-9002(95)00425-4, URL http://www.sciencedirect.com/science/article/pii/0168900295004254.

[14] K. Drozdowicz, M. Hoek, D. Aronsson, Energy calibration of neutron detectors for the neutron spectrometer TANSY, Nucl. Instrum. Methods Phys. Res. A 306 (1) (1991) 315–330, http://dx.doi.org/10.1016/0168-9002(91)90339-R, URL http://www.sciencedirect.com/science/article/pii/016890029190339R.

[15] S. Meigo, Measurements of the response function and the detection efficiency of an NE213 scintillator for neutrons between 20 and 65 MeV, Nucl. Instrum. Methods Phys. Res. A 401 (2) (1997) 365–378, http://dx.doi.org/10.1016/S0168-9002(97)01061-9, URL http://www.sciencedirect.com/science/article/pii/S0168900297010619.

[16] N. Nakao, T. Kurosawa, T. Nakamura, Y. Uwamino, Absolute measurements of the response function of an NE213 organic liquid scintillator for the neutron energy range up to 206 MeV, Nucl. Instrum. Methods Phys. Res. A 463 (1) (2001) 275–287, http://dx.doi.org/10.1016/S0168-9002(01)00260-1, URL http://www.sciencedirect.com/science/article/pii/S0168900201002601.

[17] W. Betts, F. Bieser, R. Bossingham, M. Botlo, M. Cherney, J. Chrin, P. Colarco, H. Crawford, K. Dao, H. Diaz, D.E. Greiner, L. Greiner, E.L. Hjort, S. Jacobson, R.C. Jared, E. Judd, S.R. Klein, A.N. Lebedev, M.J. LeVine, V. Lindenstruth, M.A. Lisa, K. Marks, C. McParland, T.S. McShane, J. Meier, M.T. Nguyen, D.L. Olson, I. Sakrejda, J. Schambach, R.A. Scheetz, N.T.B. Stone, C.E. Tull, G. Visser, C. Vu, H. Wieman, E. Yee, Results from the STAR TPC system test, IEEE Trans. Nucl. Sci. 44 (3) (1997) 592–597, http://dx.doi.org/10.1109/23.603717.

[18] B. Rastin, An accurate measurement of the sea-level muon spectrum within the range 4 to 3000 GeV/c, J. Phys. G: Nucl. Phys. 10 (11) (1984) 1609–1628, http://dx.doi.org/10.1088/0305-4616/10/11/017.

[19] J. Wiechula, Commissioning and calibration of the ALICE TPC, Nuclear Phys. A 830 (1) (2009) 531c–534c, http://dx.doi.org/10.1016/j.nuclphysa.2009.10.046, Quark Matter 2009. URL http://www.sciencedirect.com/science/article/pii/S0375947409007003.

[20] C. Hagmann, D. Lange, D. Wright, Cosmic-ray shower generator (CRY) for Monte Carlo transport codes, in: 2007 IEEE Nuclear Science Symposium Conference Record, Vol. 2, 2007, pp. 1143–1146, http://dx.doi.org/10.1109/NSSMIC.2007.4437209.

[21] Physical constants, Phys. Lett. B 204 (1988) http://dx.doi.org/10.1016/0370-2693(88)90508-4, IN3–127. URL http://www.sciencedirect.com/science/article/pii/0370269388905084.

[22] L. Chen, B. Blank, B. Brown, M. Chartier, A. Galonsky, P. Hansen, M. Thoennessen, Evidence for an l=0 ground state in 9He, Phys. Lett. B 505 (1) (2001) 21–26, http://dx.doi.org/10.1016/S0370-2693(01)00313-6, URL http://www.sciencedirect.com/science/article/pii/S0370269301003136.

[23] A. Horvath, J. Weiner, A. Galonsky, F. Deak, Y. Higurashi, K. Ieki, Y. Iwata, A. Kiss, J.J. Kolata, Z. Seres, J. von Schwarzenberg, H. Schelin, S. Takeuchi, S. Typel, R.E. Warner, Cross section for the astrophysical14c(n, γ)15c reaction via the inverse reaction, Astrophys. J. 570 (2) (2002) 926–933, http://dx.doi.org/10.1086/339726.

[24] D.D.S. Coupland, M. Youngs, Z. Chajecki, W.G. Lynch, M.B. Tsang, Y.X. Zhang, M.A. Famiano, T.K. Ghosh, B. Giacherio, M.A. Kilburn, J. Lee, H. Liu, F. Lu, P. Morfouace, P. Russotto, A. Sanetullaev, R.H. Showalter, G. Verde, J. Winkelbauer, Probing effective nucleon masses with heavy-ion collisions, Phys. Rev. C 94 (2016) 011601, http://dx.doi.org/10.1103/PhysRevC.94.011601, URL https://link.aps.org/doi/10.1103/PhysRevC.94.011601.

[25] J. Scherzinger, R.A. Jebali, J. Annand, K. Fissum, R. Hall-Wilton, K. Kanaki, M. Lundin, B. Nilsson, H. Perrey, A. Rosborg, H. Svensson, The light-yield response of a NE-213 liquid-scintillator detector measured using 2–6MeV tagged neutrons, Nucl. Instrum. Methods Phys. Res. A 840 (2016) 121–127, http://dx.doi.org/10.1016/j.nima.2016.10.011, URL http://www.sciencedirect.com/science/article/pii/S0168900216310361.

[26] F. Teh, Value-assigned pulse shape discrimination for neutron detectors, 2020, URL https://arxiv.org/abs/2001.07518.
[27] FARO VANTAGE Laser Trackers, URL https://faro.com/projects/3d-manufacturing/faro-laser-tracker.
[28] Costruzioni Apparecchiature Elettroniche Nucleari s.p.a. URL https://www.caen.it/.
[29] LeCroy Corporation, URL https://teledynelecroy.com/lrs/.
[30] Eljen Technologies, EJ-301, 2016, URL https://eljentechnology.com/products/liquid-scintillators/ej-301-ej-309.
[31] E. Siciliano, J. Ely, R. Kouzes, J. Schweppe, D. Strachan, S. Yokuda, Energy calibration of gamma spectra in plastic scintillators using compton kinematics, Nucl. Instrum. Methods Phys. Res. A 594 (2) (2008) 232–243, http://dx.doi.org/10.1016/j.nima.2008.06.031, URL http://www.sciencedirect.com/science/article/pii/S0168900208008772.